Molecular Crystals and Liquid Crystals Incorporating Nonlinear Optics

Publication details, including instructions for authors and subscription information:
http://www.tandfonline.com/loi/gmcl17

Photoconductivity in Mixed Stack Donor: Acceptor Crystals: Quasi One-Dimensional Electron Transport in Anthracene: Pyromellitic-dianhydride

D. Massa [a] & N. Karl [a]

[a] Physikalisches Institut der Universität Stuttgart, D 7000, Stuttgart, 80, Federal Republic of Germany

Version of record first published: 22 Sep 2006.

To cite this article: D. Massa & N. Karl (1989): Photoconductivity in Mixed Stack Donor: Acceptor Crystals: Quasi One-Dimensional Electron Transport in Anthracene: Pyromellitic-dianhydride, Molecular Crystals and Liquid Crystals Incorporating Nonlinear Optics, 175:1, 93-117

To link to this article: http://dx.doi.org/10.1080/00268948908033749

Mol. Cryst. Liq. Cryst., 1989, Vol. 95, pp. 93–117
Reprints available directly from the publisher
Photocopying permitted by license only

Printed in the United States of America

Photoconductivity in Mixed Stack Donor:Acceptor Crystals: Quasi One-Dimensional Electron Transport in Anthracene:Pyromellitic-dianhydride

D. MASSA and N. KARL

Physikalisches Institut der Universität Stuttgart, D 7000 Stuttgart-80, Federal Republic of Germany

Dedicated to Martin Pope at the occasion of his 70th birthday.

(*Received November 30, 1988*)

Improvements of the purification, material handling, and crystal growth techniques of the mixed stack donor:acceptor complex anthracene:pyromellitic-dianhydride resulted in big, high purity single crystals, which allowed us to measure a full "microscopic" (i.e. non shallow trapping-perturbed) electron mobility tensor and to study the anisotropy of the temperature dependence law of electron transport for the first time for a representative of this class of materials. These experiments reveal that electron transport is strongly anisotropic. The highest electron mobility occurs along the donor:acceptor stacking axis c, with an anisotropy of the principal axes mobilities $\mu_{33}:\mu_{22}:\mu_{11} = 256:15.5:5.0$ (in units 10^{-3} cm^2/Vs) at $T = 330$ K, and with temperature dependences $\mu_{33} \sim T^{-1.4(1)}$, $\mu_{22} \sim T^{-0.9(1)}$, and $\mu_{11} \sim T^{-0.0(1)}$. Preliminary results obtained for holes show that hole transport is thermally activated with $E_{act} = 0.58$ eV in the temperature range between 310 and 440 K for most samples, that anisotropy is small and that the *effective* hole mobilities are higher for certain directions than the respective *microscopic* electron mobilities.

INTRODUCTION

Photoconductivity in organic mixed stack donor:acceptor crystals is an interesting topic in several respects: The lowest optical excitation of the electronic system, which takes place in the visible or near UV part of the optical spectrum, is associated with nearly complete charge transfer of an electron from the donor to the intrastack next neighbour acceptor molecule(s). The question arises whether this so formed charge transfer (CT) state is a precursor of free conduction electrons and holes. If so, are then the final electron-hole separation (out of their Coulombic attraction potential) and the subsequent charge carrier transport quasi one-dimensional processes, as might be inferred from the crystallographic packing of the flat constituent molecules in linear stacks (Figure 1), and the pronounced intrastack overlap of their π-electrons? Or, as might be conjectured alternatively, is hole transport predominantly carried by the donor molecules constituting the uppermost valence

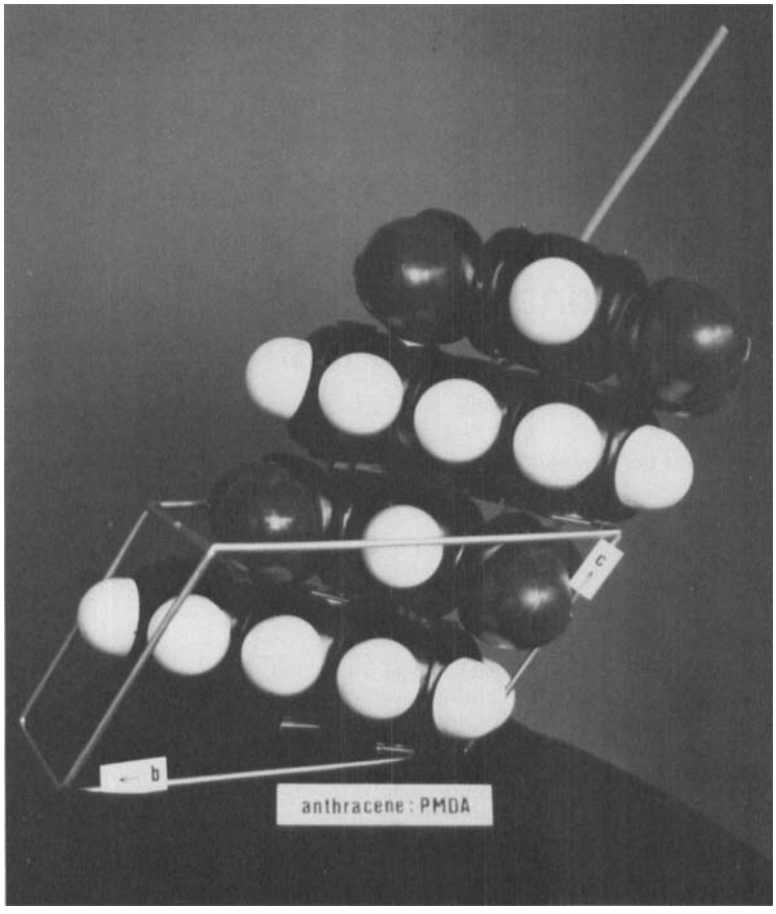

FIGURE 1 The anthracene:pyromellitic-dianhydride crystal structure, built up from atom calotte models (Leybold Company) according to the results and choice of the axes of Reference 15, but with a shift of the origin to [½ ½ 0]; the stacking axis of the planar molecules is indicated. This structure is characteristic of the great majority of weak to intermediate donor:acceptor complexes with 1:1 stoichiometry.

band by their relatively high lying highest occupied molecular orbitals (HOMOs), and electron transport by the acceptor molecules constituting the lowest conduction band by their relatively low lying lowest unoccupied molecular orbitals (LUMOs), with the consequences that hole and electron transport are two dimensional in the donor and acceptor molecular sheets, respectively, oriented essentially perpendicular to the donor:acceptor stacking direction. Which—if any—of the available theoretical models is suitable to describe charge carrier transport in such kind of *ordered* binary systems? For solving these problems clear-cut experiments were required first of all.

In the paper to be presented here, we wish to address the question of charge carrier transport in this class of materials, whereas the question of how charge carriers are generated, will be treated in a planned separate publication.

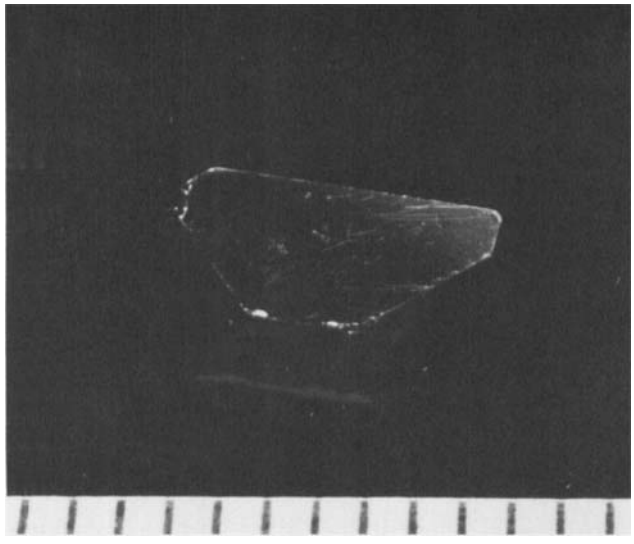

FIGURE 2 Anthracene:pyromellitic-dianhydride single crystal, grown by the plate sublimation method; scale is in mm.

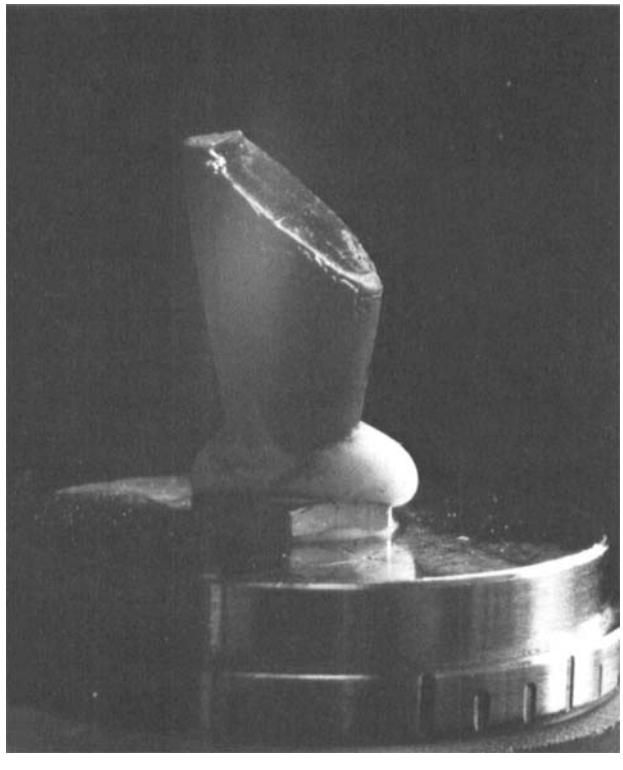

FIGURE 3 Anthracene:pyromellitic-dianhydride single crystal, grown from melt by the Bridgman method. The crystal displayed is mounted on a goniometer head to allow oriented cutting on a thread saw.

The few available data on charge carrier mobilities in photoconductive organic donor:acceptor crystals[1-3] display more or less thermally activated behaviour. We therefore conjectured that these results were still governed by multiple shallow trapping (cf. Reference 4) and, consequently, might not directly allow a more profound insight into the underlying intrinsic microscopic transport mechanism(s). This conclusion was supported by the fact that (in our opinion) none of the acceptors used so far was of really high purity. For reaching any progress in this field, the availability of higher purity crystals seemed crucial to us. Without such crystals, reliable temperature dependent anisotropic charge carrier mobilities and meaningful photogeneration data could hardly be expected.

We therefore focussed our attention on the purification problem. Whereas ultrapurification of several interesting *donor* molecules by a combination of different selected prepurification techniques with multipass zone refining is well established (see e.g. References 5–7), a suitable zone refinable (model) *acceptor* was lacking for a long time, because of the pronounced tendency of most stronger acceptors to thermally decompose at their melting point. With the successful zone refinement of the acceptor pyromellitic dianhydride (PMDA)[9] which has a fairly big solid state electron affinity of approximately 3.6 eV,[10] an important first step had been made, which had led for the first time to an indication of an *unactivated* temperature dependence of the electron mobility $\mu \sim T^n (n = 0 \ldots -2)$ in the 1:1 complex with anthracene, A:PMDA.[8] It appeared reasonable, therefore, to pick up this system once again and to try to further improve the purification and crystal growth procedures. This was indeed successful and allowed us to measure the full *microscopic* electron mobility *tensor* in a considerable temperature interval. These results, together with some preliminary results on hole transport, shall be presented and discussed here.

EXPERIMENTAL

Commercial PMDA powder was filled into a glass tube and subjected to a heat pretreatment, consisting of slowly raising its temperature up to the melting point under continuous pumping by a mechanical vacuum forepump; this process removes traces of the free acids (which form under the natural humidity of air) by transforming them to the dianhydride. Several fast passages of a single *wide* molten zone (*offering a large transport volume*) were subsequently applied to the brown product in order to quickly get rid of the main part of the impurities, before these cause appreciable decomposition. From then on normal zone refining techniques (cf. References 5–7) are applicable. After ca. 100 zone passages the material of the central part of the zone refining tube was combined with that of a similar second zone refining tube, and refined by another 100 zone passages; this latter tube carried a vacuum break seal, through which finally several storage ampoules, blown on, were filled under vacuum by sublimation in fractions. These ampoules, equipped with a break seal for later use, were sealed off with a flame. Anthracene was vacuum-sublimed and zone refined in the conventional way, cf. References 5–7.

Further zone refining (180 zone passages) was then performed with an equimolar (1:1) mixture of anthracene and PMDA. This *complex zone refining*[11] is possible because the red 1:1 complex melts congruently; it serves to establish the exact stoichiometry and to further decrease the level of residual impurities.

For crystal growth after the Bridgman method a double Liebig condenser furnace was used (cf. Reference 5a); the upper and lower Liebig condensers were heated to 246 and 226°C, respectively, by pumping oil from two high temperature oil bath thermostates through them. In order to keep thermal decomposition as small as possible, care was taken not to exceed 6 degrees above the melting point (240°C). For the liquid/solid phase boundary of the growing crystal it was found to be optimal to lie at the greatest slope of the temperature gradient (1.4 deg/mm). Crystal growth was accomplished by slowly lowering the ampoule (0.34 mm/h) into the lower half of the "oven", which was internally filled with oil for better thermal contact to the ampoule. This oil level was counterbalanced to stay at a constant level during immersion of the ampoule. After growth the crystal was slowly cooled down during one week. A Bridgman-grown A:PMDA single crystal, mounted (with Torrseal, Varian) on the goniometer head of a thread saw, is displayed in Figure 2.

Crystal growth by the plate sublimation method was performed as described before[8,5a]; an example of a sublimation-grown crystal is depicted in Figure 3.

The A:PMDA crystals display cleavage parallel to the [001] stacking direction along the two different crystallographically inequivalent planes, (010) and $(1\bar{1}0)$; with plane parallel cleaved slices between crossed polarizers and visible light $\lambda > 630$ nm, these two situations can be distinguished by their different "inclined extinction" at angles 22° and 28°, respectively, relative to the [001] intersection edge of these two cleavage planes. Through the plane of perfect cleavage, $(1\bar{1}0)$, one of the three principal axes of the optical tensor (indicatrix) is nearly perpendicular (crossed isogyres in a conoscopic view), whereas through the (010) cleavage plane, which is less clearly expressed, one of the two optical axes is visible at the periphery of the image field with strong colour dispersion of the (single) isogyre.[12] These features allow preorientation of the crystals under a polarization microscope to $\pm 5°$. Thin slices (0.4–0.5 mm) were then cut off (gently, i.e. by dissolution rather than by mechanical abrasion) on a thread saw with a xylene-wetted polyester thread, and polished down to $d \sim 0.2$ mm on xylene-wetted lens cleaning paper on a flat glass plate with a 50 mm diameter micrometer polishing head. A thickness homogeneity $\Delta d/d \lesssim 3\%$ could be obtained for most samples. These samples were subsequently checked under a polarization microscope for single crystallinity, or for discrimination and selection of the major single crystalline regions, and placed into a high vacuum chamber immediately after for dessication (at $2 \cdot 10^{-5}$ hPa for 12 hours). Finally semitransparent silver electrodes were deposited by vacuum evaporation.

The precise orientation of each sample was determined by x-ray diffraction; however, to avoid trap formation by radiation damage, only after completion of the electrical measurements. The transmission "Laue live" technique, in combination with computer-calculated diffraction patterns, as described elsewhere,[13] proved

extremely helpful for orienting these triclinic samples, lacking any useful symmetry element. A Laue photograph at perpendicular incidence of the parallel X-ray beam to the surface of the crystal slice (precisely adjusted by a counterpropagating He/Ne laser beam) was finally made, and the theoretical Laue diffraction pattern varied on a computer (crystal lattice rotation and fine adjustment of the exposure distance) until simultaneous full coincidence with all reflections on the photograph was reached, cf. Figure 4, a result which could easily be checked by superposition of the two diffractograms on a light box. The sample slices used for the electric transport measurements to be described here had the orientations (of their plane normal vectors $\mathbf{L}$, $|\mathbf{L}| = 1$) marked in the stereographic projection of Figure 5.

For the electrical measurements these samples were sandwiched between an electrically conductive (indium/tin-oxide–covered) fused silica disc, which was gently pressed on, and a temperature-controlled copper support, in a home-made nitrogen gas flow cryostate/thermostate. Intimate thermal contact to the copper support was achieved by a droplet of a liquid In/Ga alloy. For measurements above 300 K purified dry nitrogen (of ambient pressure) was admitted to keep sublimation of the organic crystal down; below 300 K the cryostate was evacuated for better thermal insulation.

Charge carrier mobilities were measured by the time-of-flight technique in a similar way as described in Reference 6 by using strongly absorbed light of a home-made atmospheric pressure nitrogen laser ($\lambda = 337$ nm, $\tau_L = 0.8$ ns FWHM) for the optical charge carrier generation near the semitransparent front electrode. The time-of-flight pulses were picked up by a low noise cathode follower probe (Tektronix P 170 CF) at a suitable load resistor ($50\ \Omega \leq R \leq 9\ M\Omega$) which was individually chosen such as to make a good compromise between the required time resolution, magnitude of the signal, and signal to noise ratio. The amplified (Tektronix 1121) signals were displayed on an oscilloscope (Tektronix 7904 + 7A19 + 7B15) and photographed.

In the time-of-flight pulses the arrival time τ of the drifting charge carrier "sheet" was determined from the kink of the pulses (arrows in Figure 6, which displays typical negative electron time-of-flight pulses in the two different temperature regimes which we will have to distinguish). To the relative error span of the so obtained flight times ($\pm$ 2 . . . 5%) twice the relative error in the sample thickness, $2 \cdot \Delta d/d$, caused by thickness inhomogeneities Δd has to be added in the evaluation of the drift mobility "parallel to the given field direction," $\mu_{\|} \pm \Delta\mu_{\|}$ (which is the actually measured sample property, defined as velocity component parallel to the electric field divided by the magnitude of the field, see below).

An important point with time-of-flight mobility measurements is always to check whether (at least for not too high fields) Ohm's law, i.e. a linear relation between the applied electric field strength and the observed charge carrier velocity $v = d/\tau$, holds; otherwise the normal definition of a mobility as a material property fails. An especially thorough check is represented in Figure 7 as an example. Moreover, the absence of any ordinate intercept in Figure 7 clearly demonstrates the absence of any internal field caused by resident space charge, another possible source for unreliable results.

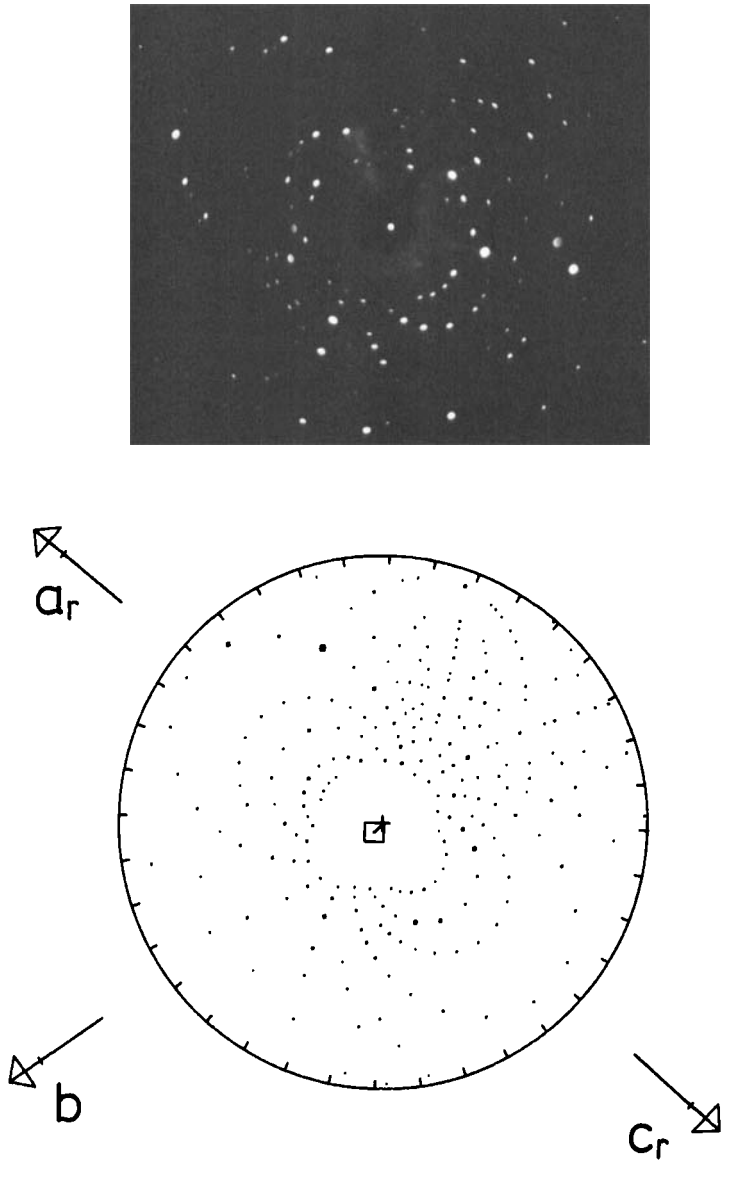

FIGURE 4 Experimental (a) and computer generated (b) X-ray Laue diffraction pattern for one of the crystal slices (no. 5), for which mobility data were measured and used to contribute to the evaluation of the electron mobility tensor. The calculation was confined to an aperture angle of 62.1° and to reflections with Miller indices up to (575), of which the 296 strongest were plotted; the best fit of the calculated to the experimental diffraction pattern was obtained with orientational angles $\alpha = 124.2°$, $\beta = 94.3°$, and $\gamma = 34.5°$ with respect to orthogonal coordinates axes x,y,z with $z \| c$, $y \| (c \times a)$ and $x \| (c \times a) \times c$; this corresponds to Miller indices (1045 $\overline{1499}$ 1000) of the surface plane of the slice in the triclinic crystallographic coordinate system. The axes a, b, and c are parallel-projected and marked by the index r when they point in the reverse direction, i.e. off the observer. The relative intensities of the calculated Laue reflections are represented by the area of the respective square symbol (when it exceeds the minimum pixel size); the strong reflection near the center of the calculated pattern is obscured by the primary beam stopper in the photograph (a); (the primary beam was admitted for 1/1000 of the exposure time only). Due to the residual *characteristic* lines in the 30 kV tungsten X-ray spectrum the experimental intensities can occasionally deviate from the calculated ones.

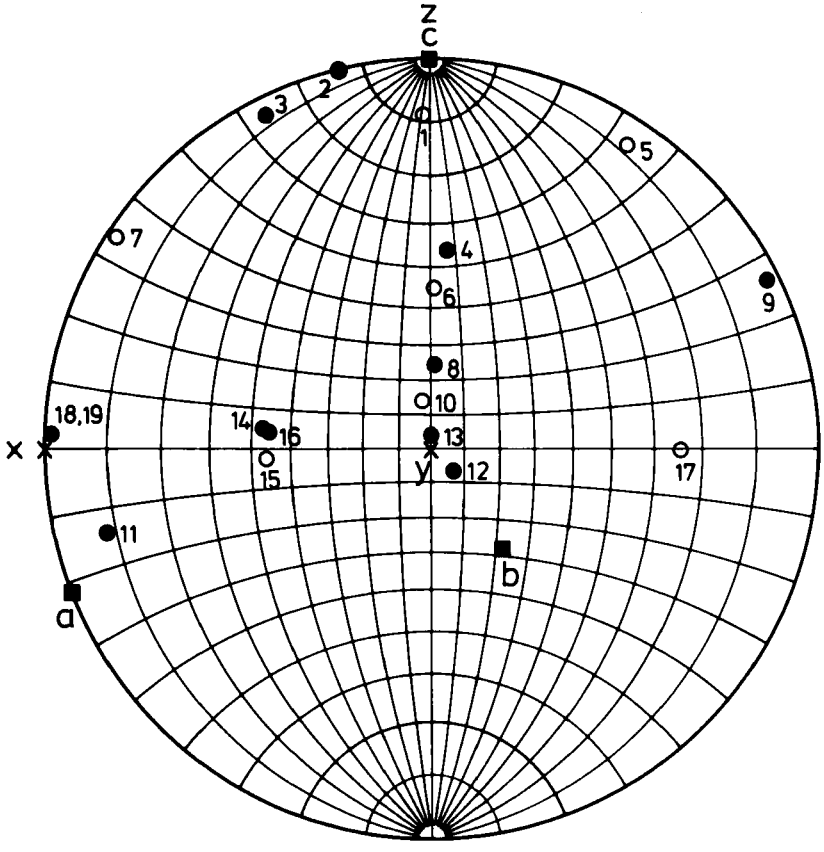

FIGURE 5 Collection of the directions for which electron mobilities were measured in A:PMDA; the normals to the individual crystal slices, labelled by numbers, are marked in stereographic projection; projection plane is the crystallographic (010) plane. The open symbols indicate directions pointing into the lower half space. The directions of the crystallographic axes a, b, and c of the triclinic lattice are marked by solid squares. Orthogonal axes x,y,z as used in this paper (cf. caption of Figure 4) are indicated by crosses; z is parallel to c.

RESULTS

Primary Experimental Data, Electrons

Examples of the experimentally obtained electron mobilities, plotted as log μ versus log T are presented in the Figures 8–11. Table I gives a compilation of the mobilities at 430 K, the slope n, (corresponding to the exponent of a $\mu \sim T^n$ fit in the high temperature regime of the data), and the thermal activation energy E_{act} in the low temperature regime, for samples which could be measured down to sufficiently low temperatures to allow a fit by the Hoesterey-Letson model of multiple shallow trapping-limited transport,[4]

$$\mu_{eff} = \mu\{1 + c_{tr} \exp(E_{act}/kT)\}^{-1}, \quad (1)$$

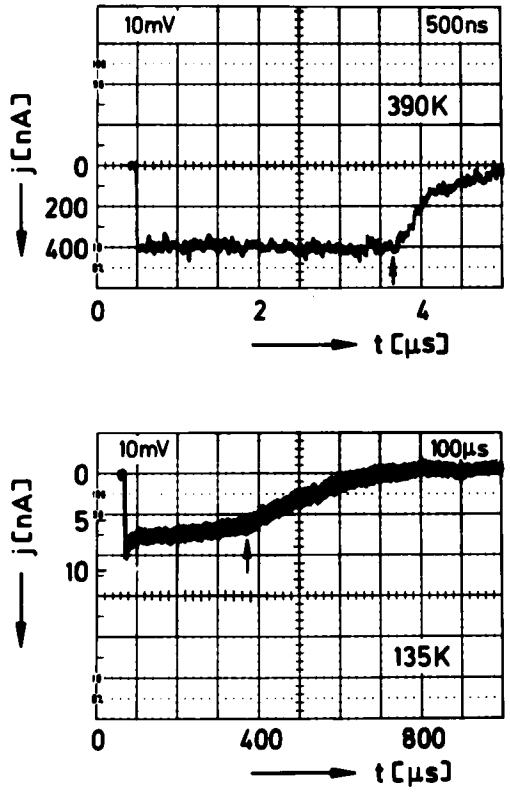

FIGURE 6 Typical electron time-of-flight current pulses (sample 5, thickness L = 0.192(5) μm) in the high and low temperature regime. Electric field strength was 42 kV/cm in (a), and 73 kV/cm in (b). While the pulse at 390 K has the near to ideal rectangular shape, that obtained at 135 K displays a strong dispersion, i.e. a broad distribution of the arrival times, which are considerably longer than in (a).

as indicated by the dashed lines in Figures 8 and 9; (c_{tr} is the ratio of trapping states to band states, generally interpreted as "trap concentration" of one single kind of trap with thermal activation energy E_{act}, which is often called "trap depth," although it may be larger than the mere energetic trap to band distance). Before entering a detailed discussion of the transport properties below, we wish to point out three essential findings:

I) There is an appreciable temperature range where transport is not limited by multiple shallow trapping; rather a "microscopic" transport behaviour appears with a power law increase of the electron mobility with decreasing temperature (at least for several orientations).

II) For certain orientations (near the x or a axis) the electron mobility is (intrinsically) nearly temperature independent.

III) In the higher temperature regime, exhibiting intrinsic ("microscopic") electron mobility, a very great anisotropy occurs, with the highest mobilities along the c stacking axis, cf. Table I and Figure 5.

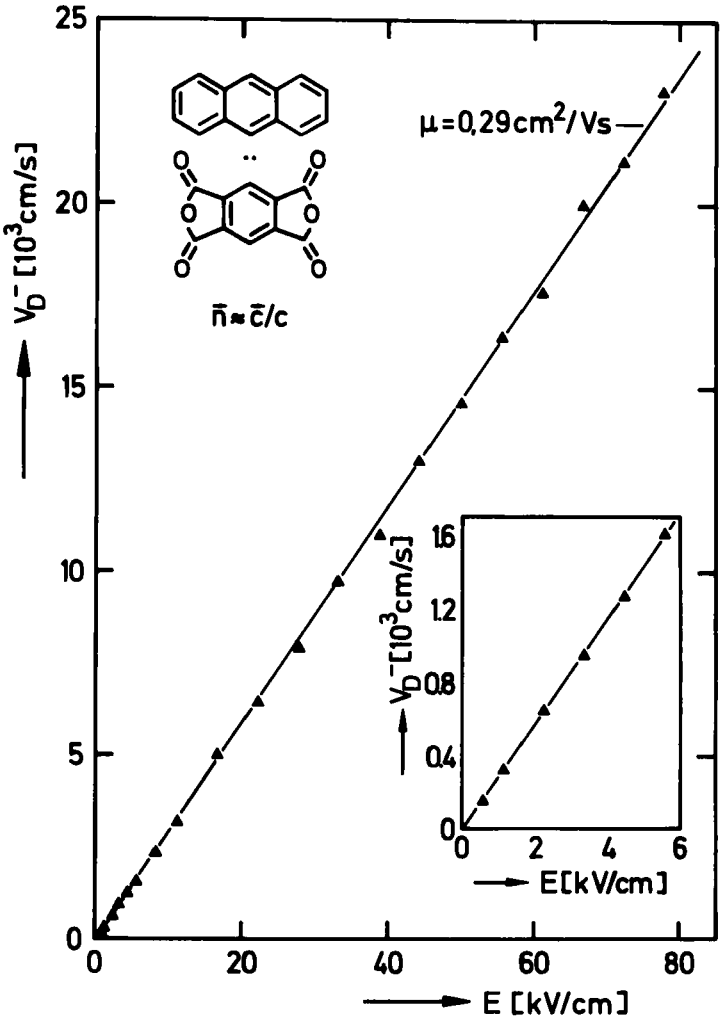

FIGURE 7 Electron velocity versus electric field strength at $T = 300$ K for a sample cut perpendicular to the stacking direction [001]. The straight line through the origin demonstrates linear transport up to 80 kV/cm and absence of distortions by space charge-generated internal fields.

Evaluation of the electron mobility tensor

The temperature dependent mobility data $\mu_{\parallel}^{n}$ of 17 samples† ($n = 1 - 17$) of orientations $L^n = (l_1^n, l_2^n, l_3^n)$ obtained with electric fields $E \parallel L$ as

$$\mu_{\parallel} = \frac{v_{\parallel}}{|E|} = \frac{vL}{|E|} = \frac{(\mu E)L}{|E|} = (\mu L)\cdot L \qquad (2a)$$

†The samples no. 1, 3–16, 18, 19 of Figure 5 and Table I were cut from two good Bridgman crystals; samples 2 and 17 originated from a third crystal of slightly inferior quality/purity; the data of the latter were therefore excluded from the tensor evaluation.

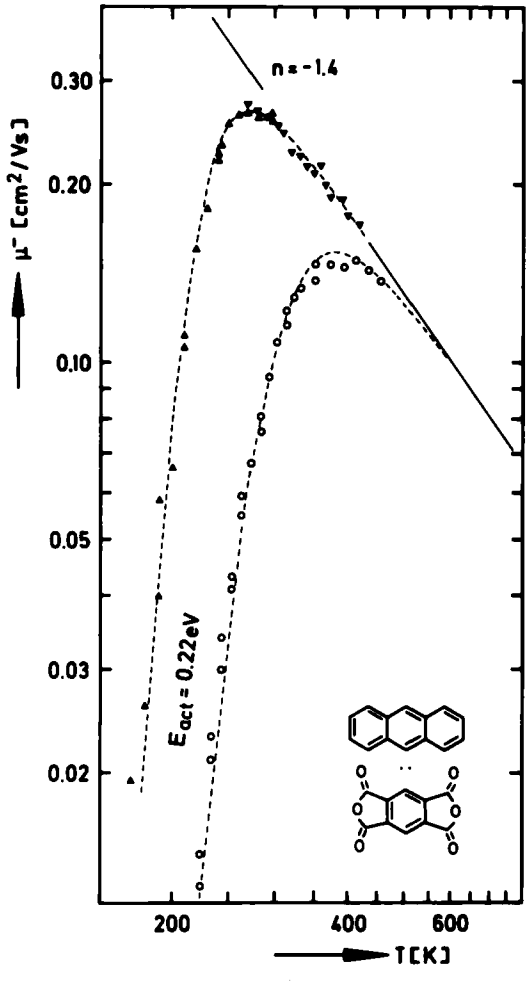

FIGURE 8 Electron mobility for the electric field approximately parallel to the stacking direction c of the Bridgman-grown sample 2 (solid triangles), in comparison with earlier results,[8] obtained with a sublimation-grown crystal (open symbols). Progress in purification is indicated by the fact that the microscopic behaviour, $\mu \sim T^{-1.4}$ extends down to lower temperatures and thus leads to higher mobilities in the higher purity material obtained in the present work. A Hoesterey-Letson fit[4] (dashed curve) indicates a shallow electron trap with the same activation energy, 0.22 eV, in both (completely independent) samples, but with a concentration reduced from $5 \cdot 10^{-4}$ to $5 \cdot 10^{-5}$ mole/mole in the present samples.

or, in index notation for the sample n:

$$\mu_{\parallel}^{n} = \mu_{ij} l_i^n l_j^n \tag{2b}$$

were used to calculate a best tensor by a least squares matrix algorithm (cf. for instance Reference 14; the l_i^n are the directional cosines of the normal to the slice n with respect to the axes of the chosen reference coordinate system). Briefly, the procedure is as follows:

Let $\mu = \mu_{ij}$ be the true (but unknown) material property tensor, consisting, in general, of six independent components (μ_{ii}, $\mu_{ij} = \mu_{ji}$, $i = 1 \ldots 3, j = 1 \ldots 3$); then for the given direction L^n the value $\mu_{\parallel}^n = \mu_{ij} l_i^n l_j^n$ is expected, but—owing to experimental errors—not obtained; rather, an error $v^n = \mu_{\parallel}^n - M^n$ occurs; M^n is the value actually measured for the direction n. Replacing in μ_{ii} and in the

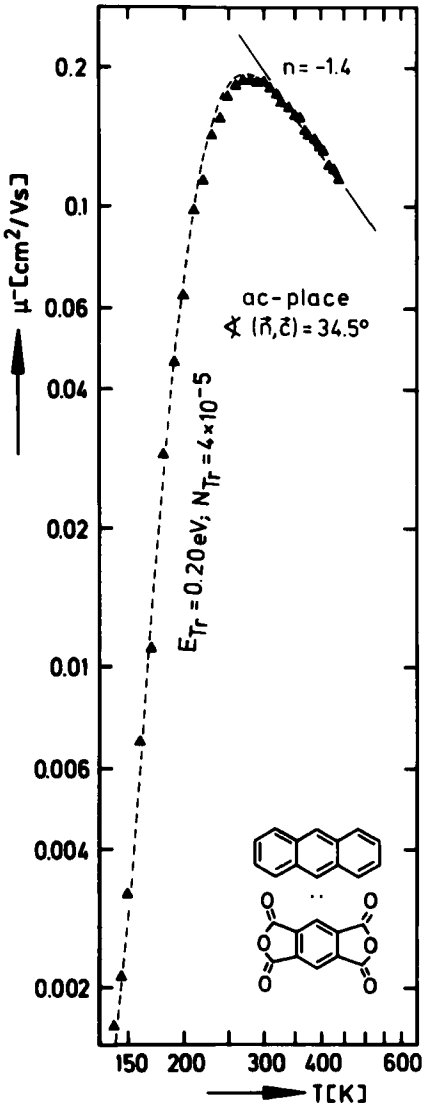

FIGURE 9 Electron mobility for the electric field in the *a-c* plane, 34.5° off the *c* stacking direction, sample 5. Temperature dependence is still $\mu \sim T^{-1.4}$. Notice the drastic reduction of the mobility by more than two orders of magnitude in the low temperature regime, which is caused by the residual shallow electron trap of a molar concentration of only 40 ppm, as obtained by a Hoesterey-Letson fit[4] (dashed line).

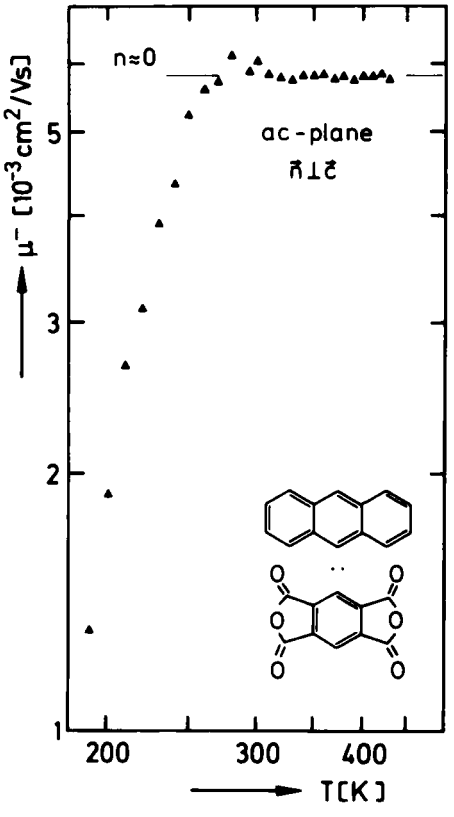

FIGURE 10 Electron mobility for the electric field perpendicular to the c stacking axis and in the a-c plane, close to the x axis of the orthogonal coordinate system (sample 18): within the experimental scatter electron transport is temperature independent from 260 to 440 K.

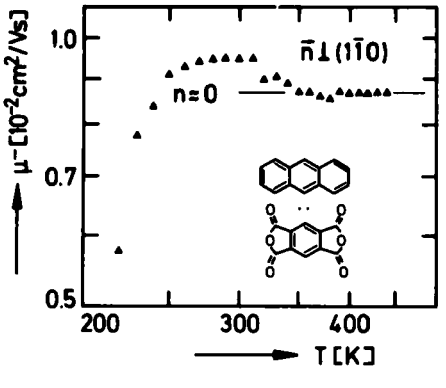

FIGURE 11 Electron mobility for the electric field perpendicular to the c stacking axis and perpendicular to the (1$\bar{1}$0) cleavage plane (sample 17): indications of a transition from a $\mu \sim T^{o}$ to a $\mu \sim T^{n}$ ($n < 0$) behaviour.

TABLE I

Overview on the experimental parameters of the individual samples used for the measurements and on some principal results: electron mobility component parallel to the electric field vector for the electric field perpendicular to the surface of the respective sample slice, at 430 K, $\mu_{430\,K}$, together with the exponent n of the $\mu \sim T^n$ dependence found for the "high temperature regime," and thermal activation energy E_{act} for the "low temperature regime." For the orientations see Figure 5. The electric field strength applied to these samples was varied between 2.6 and 120 kV/cm; no indications of nonlinear (non-Ohmic) transport could be observed for any sample.

Sample no.	μ^-(430 K) [cm²/Vs]	n	E_{act} [eV]	Measured temp. Range [K]
1	0.163*	−1.4(1)	0.19(1)	150–400
2	0.165(5)	−1.4(1)	0.21(1)	160–450
3	0.16	−1.3(1)	0.19(1)	140–430
4	0.127	−1.4(1)	0.19(1)	100–430
5	0.120	−1.47(5)	0.17(1)	100–440
6	0.11	−1.4(1)	0.20(1)	110–430
7	0.055	−1.5(1)	—	85–430
8	0.045	−1.1(2)	0.19(1)	110–430
9	0.045	−1.50(5)	0.21(1)	140–440
10	0.027	−1.5(2)	0.16(1)	100–440
11	0.0150	−1.0(1)	0.24(1)	140–440
12	0.0144	−1.2(1)	0.19(1)	140–430
13	0.013	−1.3(2)	—	230–430
14	0.0105	−0.7(1)	0.23(1)	150–440
15	0.010	−0.7(1)	0.21(1)	160–440
16	0.0088	−0.7(1)	—	190–440
17	0.0087	≈ 0	—	210–440
18	0.0055	≈ 0	—	180–440
19	0.0054	≈ 0	—	210–440

*extrapolated

product $l_i l_j$ the combinations of indices i,i by $k = 1 \ldots 3$, and $i,j (i < j)$ by $k = 4 \ldots 6$ leads to

$$\nu^n = \Lambda_k^n \mu^k - M^n \tag{3}$$

where Λ_k^n stands for $l_i^n l_j^n$. Equation (3) can be considered as a matrix equation relating the single column matrix μ^k of the 6 ($k = 1 \ldots 6$) components of the searched mobility tensor via a $n \cdot k$ orientation matrix Λ_k^n to the single column matrices M^n (of the n measured $\mu_\parallel$ values) and ν^n (of the n errors). For $n > k$ the equation system (3) is overdetermined; by demanding the sum of the squared errors, $\nu_n \nu^n$, to assume a minimum with respect to the searched best set of μ^k values (considered as variables to be optimized), i.e. requiring $\nu^n \partial \nu^n / \partial \mu^k \stackrel{!}{=} 0$, leads to the solution for the components of the best tensor (in matrix notation)

$$\mu = (\Lambda_t \Lambda)^{-1} \Lambda_t M \tag{4}$$

where Λ_t means the transposed matrix.

So far (following Reference 14) the errors were treated in a similar way for all crystallographic directions; however, since we know already that the tensor is very

anisotropic, the question arises whether in Equation (3) the assumption of a weighted error might more appropriately describe the experimental situation (otherwise small errors made in fast directions can completely dominate and thus seriously distort the result of the least squares fitting in slow directions). From the way the flight times are determined, it is suggestive to take the relative errors v^n/M^n as given, and to operate with these in the equation system (3); the Λ orientation matrix thus requires a detailed normalization by division of row n through M^n in each of its n rows; since $M^n = M^n(T)$, this has the consequence that the so defined new orientation matrix now needs recalculation at each temperature!

The best tensors thus obtained for each temperature were subject to a principal axis transformation; the results are plotted in Figure 12. The numerical tensor data for three temperatures in the high temperature regime and the orientation matrices of the respective principal axes are collected in Table II. With the best tensor fitting of the experimental set of data it is possible to calculate (cf. Reference 14) the deviations of each measured $\mu_{\|}^n$ from that value which the best tensor predicts. For this purpose the components of the best tensor have to be inserted into Equation (3). The error matrix v^n (in relative units of the respective $\mu_{\|}^n$) so obtained gave errors $\Delta\mu/\mu$ of only ~ 0.05, except for one direction where it was 0.1. This is an excellent proof for the reliability of *all* measurements used for the tensor evaluation.

TABLE II

Electron mobility tensor; results of the least squares fit of a best tensor to the experimental data obtained in 17 series of temperature dependent mobility measurements in the directions (1, 3–16, 18, 19) marked in the stereographic projection of Figure 5. For the definition of the x, y, z coordinates see caption of Figure 4.

		T = 330 K	T = 380 K	T = 430 K
tensor components [10^{-3}cm^2/Vs]	μ_{xx}	5.1	4.9	5.2
	μ_{yy}	15.4	14.1	12.3
	μ_{zz}	265	224	186
	μ_{yz}	−0.214	−0.67	1.25
	μ_{xz}	−0.80	−0.89	−1.56
	μ_{xy}	−0.80	−0.62	−0.76
principal components [10^{-3}cm^2/Vs]	μ_{11}	5.0	4.9	5.1
	μ_{22}	15.5	14.1	12.4
	μ_{33}	265	224	186
directions of the principal axis [deg.]	α_{11}^x	4.4	3.9	5.9
	α_{11}^y	85.6	86.2	84.1
	α_{11}^z	89.8	89.8	89.5
	α_{22}^x	94.4	93.8	95.9
	α_{22}^y	4.4	3.8	5.9
	α_{22}^z	90.0	89.8	90.5
	α_{33}^x	90.2	90.2	90.5
	α_{33}^y	90.0	90.2	89.6
	α_{33}^z	0.2	0.3	0.6

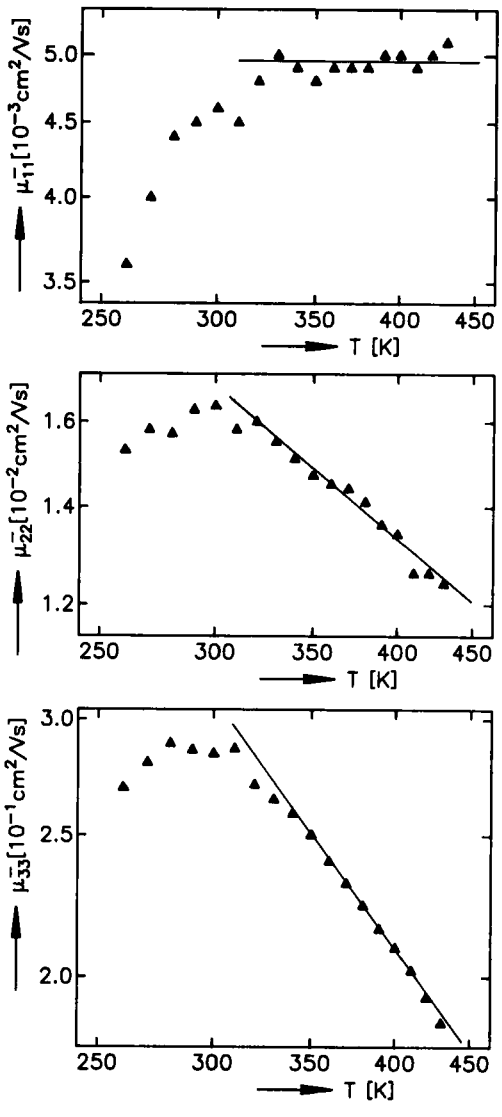

FIGURE 12 Principal components of the electron mobility tensor in anthracene:PMDA as a function of temperature, log μ versus log T plot with the same logarithmic scaling used on all axes. These data were obtained by a least squares fit of a best tensor to the experimental results of 17 series of temperature dependent time of flight measurements in different directions. Within the experimental uncertainty $\mu_{11} \sim T^{0.0(1)}$, $\mu_{22} \sim T^{-0.9(1)}$, $\mu_{33} \sim T^{-1.4(1)}$ in the temperature range 320–430 K where multiple shallow trapping influences can be neglected. The greatest mobilities, $\bar{\mu}_{33}(T)$, are observed in the c stacking direction, the smallest, $\bar{\mu}_{11}(T)$, in the a-c plane in a direction perpendicular to c.

Primary experimental data, holes

Typical hole mobility results, as obtained from time-of-flight measurements by reversing the electric field (cf. Figure 14), are presented in Figure 13 in a $\log\mu$ versus $1/T$ Arrhenius plot, and compared with the electron mobilities for the same direction. First of all, it appears that the hole mobility is thermally activated with a much bigger activation energy than the electron mobility (in the low temperature regime of the latter); secondly, it is obvious that the hole mobility, though multiple shallow trapping limited, can exceed the microscopic electron mobility (e.g., for the sample orientation of Figure 13, in the temperature range above 410 K). More hole mobility data are collected in Table III.

Evaluation of the hole data

All hole mobilities obtained with these Bridgman crystals were found thermally activated with $E_{act} \sim 0.58$ eV in the entire temperature range where measurements were possible (the upper temperature limit was dictated by the onset of sublimation). Under the assumption of little scatter of the hole trap concentrations among the samples used (which is justified because most samples were cut from a narrow region of one single Bridgman crystal) each measured mobility μ_{eff} should be proportional to the microscopic mobility μ (cf. Equation (1)) of the respective direction by the same proportionality factor; therefore these thermally activated mobilities should reflect the anisotropy of the *microscopic* hole mobility tensor, and it can be concluded from these data that the hole mobilities are much more isotropic ($\mu^+_{max}:\mu^+_{min} = 5:1$), than the electron mobilities ($\mu^-_{max}:\mu^-_{min} = 40:1$), at 400 K. A tentative tensor evaluation gave for of the tensor matrix $\mu^k = \mu^+_{ij}$ in the x,y,z coordinate system the elements (in units [10^{-2} cm^2/Vs]):

$$\mu_{xx} = 0.79,\ \mu_{yy} = 2.85,\ \mu_{zz} = 0.85,\ \mu_{xy} = -0.07,\ \mu_{yz} = -0.15,\ \mu_{xz} = -0.28$$

and an error matrix (as defined above, in relative units):

$$v^n = (-0.08,\ 0.05,\ 0.40,\ 0.01,\ 0.06,\ 0.04,\ -0.15,\ -0.05,\ -0.09,\ 0.02)$$

for the directions no. (1, 4, 6, 7, 8, 9, 10, 11, 12, 16).

The principal axis (of the effective hole mobility tensor) with the highest mobility, $\mu^{eff}_{22} = 2.9\cdot10^{-2}$ cm^2/Vs, lies between the y and the b axis (4° off y, cf. Figure 5); that with the smallest ($\mu^{eff}_{11} = 0.5\cdot10^{-2}$ cm^2/Vs) at $\sim$ 45° to x and z (90° to y), and the intermediate ($\mu^{eff}_{33} = 1.1\cdot10^{-2}$ cm^2/Vs) orthogonal to these two.

An estimate of the hole trap concentration from the temperature depending μ^+_{eff} and approximate microscopic μ^+-values (see below) by using the Hoesterey and Letson formula, Equation 1, leads to the very small value of $c^+_{tr} \leq 10^{-6}$ mol/mol, which demonstrates the achieved high purity of the material. Nevertheless this trap exhibits great efficiency in reducing the average hole velocities; this is a consequence of its relatively great depth (cf. Equation 1).

As a preliminary result we wish to also mention that samples cut from some of the sublimation-grown crystals, for which extremely extensively zone-refined an-

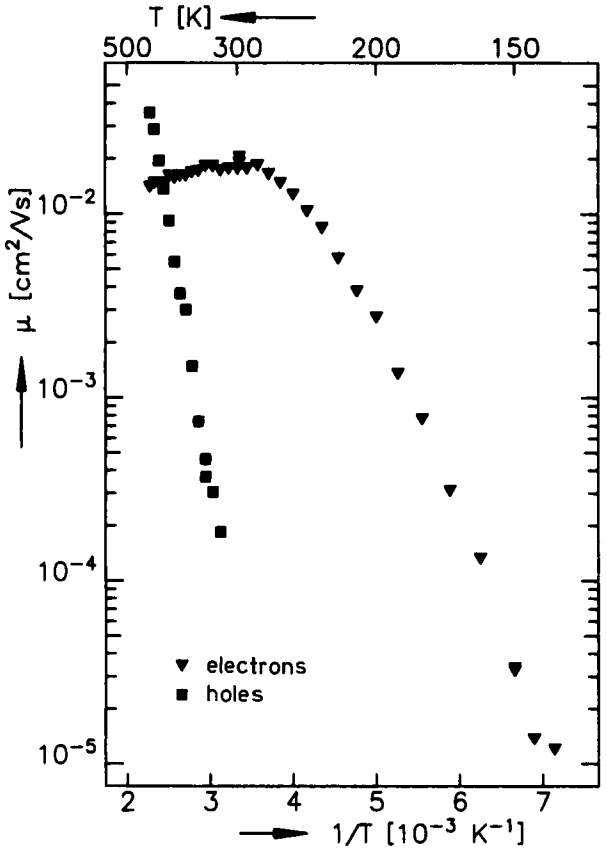

FIGURE 13 Hole mobility near the crystallographic *a* axis (sample 11), solid squares, plotted as log μ versus $1/T$; hole transport is fully thermally activated (multiple shallow trapping-limited, $E_{act} = 0.57$ eV); it nevertheless exceeds the microscopic electron mobility for temperatures above 410 K. It can therefore be concluded, that *microscopic* hole transport is considerably faster than electron transport for this direction.

TABLE III

Overview on the results of hole mobility measurements with Bridgman-grown anthracene:PMDA crystals. The electric field strength applied ranged between 20 and 50 kV/cm.

Sample no.	Measured temp range	μ^+(400 K) [cm²/Vs]	E^+_{act}[eV]
1	380–400 K	$8.5 \cdot 10^{-3}$	—
4	350–420 K	$1.5 \cdot 10^{-2}$	0.60
6	370–430 K	$3.3 \cdot 10^{-2}$	0.57
7	340–430 K	$5.7 \cdot 10^{-3}$	0.56
8	380–430 K	$2.6 \cdot 10^{-2}$	0.62
9	340–440 K	$1.1 \cdot 10^{-2}$	0.60
10	310–400 K	$2.4 \cdot 10^{-2}$	0.59
11	320–440 K	$9.1 \cdot 10^{-3}$	0.57
12	405–425 K	$2.6 \cdot 10^{-2}$	—
16	370–426 K	$1.7 \cdot 10^{-2}$	0.55

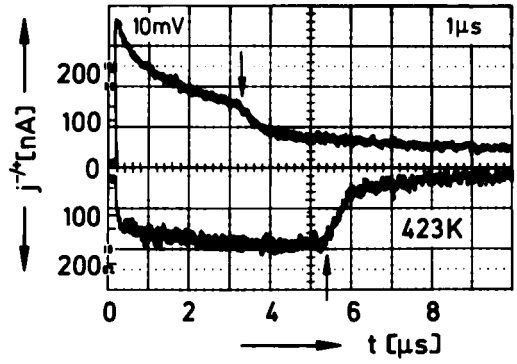

FIGURE 14 Hole and electron transit pulses obtained with a crystal slice cut from a sublimation grown anthracene:PMDA crystal, oriented approximately perpendicular to the *c* stacking axis (i.e. $E \| c$), L = 0.202 mm, E = 50 kV/cm. In the positive (hole) and in the negative (electron) pulse the kink indicates the respective transit time of *microscopic* transport; in the hole signal a long tailing occurs which is caused by those holes which were subject to multiple shallow trapping limited transport.

thracene had been used (950 zone passages) and no extra complex-zone-refining had been applied, displayed a non-thermally activated transport behaviour. These samples, cut for observing $\mu^+_{\|c}$, were still too small in area for precise measurements, but μ^+_{cc} was approximately twice μ^-_{cc} and proportional to T^n, $n < -1$ between 340 and 440 K for very few samples. (The electron mobilities obtained with these samples and with other sublimation-grown crystals were not substantially different from those obtained with Bridgman crystals.)

DISCUSSION

Electron transport

We here wish to enter a more qualitative discussion of the electron and hole mobility results only, because proved models appropriate for a description and interpretation of the room temperature mobilities in organic molecular crystals are not available presently (cf. e.g. Reference 6). Two extreme situations might have been considered for making a prediction on the nature and the underlying states of electron transport in a mixed stack donor:acceptor complex like anthracene:PMDA:

I) There is general agreement that in molecular crystals composed of *aromatic* i.e. *π-electron carrying* molecules charge carrier transport is based on intermolecular *π-electron interactions* and that transport therefore occurs in π-electron states (cf. e.g. References 16 and 17). The geometric π-electron overlap in *mixed stack donor:acceptor crystals* is undoubtedly largest between the intrastack next neighbour donor and acceptor molecules (anthracene, and PMDA, respectively, in our example). The distance between successive molecular planes in the stacking direction is smaller and/or the percent area overlap greater than in a typical neat donor crystal (like e.g. anthracene) along the *a* or *b* (pseudo-) stacking directions.

TABLE IV

Comparison of electron mobilities along molecular stacking or pseud-stacking directions of anthracene:PMDA and several one-component molecular crystals (at 300 K). The term "pseudo-stacking" is used whenever the inclination angle of the normal to the molecular plane with respect to the considered stacking direction is greater than in usual donor:acceptor stacks. (The numerical data are taken from Reference 18; φ (durene) was calculated from the atomic coordinates of Reference 20.)

	Stacking type	Stacking vector [Å]	Inclination angle φ [deg]	Electron mobility [cm²/Vs]	Temperature dependence $\mu \sim$
durene	pseudo-	$b = 5.77$	67	$\mu_{bb}^{-} = 8$	$T^{-2.5}$
perylene	pseudo-, dimerized	$b = 2 \times 5.41$	55	$\mu_{bb}^{-} = 5.5$	$T^{-1.7}$
anthracene	pseudo-	$b = 6.04$	64	$\mu_{bb}^{-} = 1.05$	$T^{-0.84}$
anthracene :PMDA	mixed	$c = 7.32$	21	$\mu_{cc}^{-} = 0.3$	$T^{-1.4}$

In these latter substances the room temperature electron mobilities are typically around 1 cm²/Vs with $\mu \sim T^{-1.5}$ (cf. Reference 18 and the examples in Table IV). For the closer packed donor:acceptor stacks an intrastack electron mobility μ_{cc}^{-} much greater than 1 cm²/Vs would have been expected from that argumentation. This is not the case, though the temperature dependences are comparable.

II) On the other hand, from the solid state electron affinities of anthracene (~1.8 eV[18]) and PMDA (~3.6 eV[19]) it is clear for energetic reasons that an excess electron should reside predominantly on the lowest unoccupied molecular orbital, LUMO, *of the acceptor* (PMDA), and that the conduction states (or conduction band) should essentially be made up of PMDA states, therefore, with only small admixtures of the at least 1.8 eV higher anthracene states. Thus one could have expected alternatively that on-stack electron transfer should occur essentially from acceptor to acceptor, i.e. over twice the donor:acceptor distance (together c = 7.12 Å) by tunnelling through the donor, which offers no resonant states. If we again compare this situation with the electron transport in b-direction of neat anthracene (b = 6.04 Å), these situations are geometrically comparable and a similar or slightly smaller mobility μ_{cc}^{-} would have been predicted than for anthracene, with a similar temperature dependence. This is semiquantitatively so found for anthracene:PMDA, indeed, and also fits into the line of the other substances listed in Table IV.

The argumentation is, admittedly, a rather heuristic one. The different inclination angles of the molecules with respect to the considered stacking direction, their lateral interactions and their chemical differences (size and topology of the π-electron system, influences of ligands) render a quantitative comparison a nearly unsolvable task. Nevertheless, the experimental results are strongly in favour of the second model, assuming that electrons move essentially on acceptor states (holes on donor states), with the consequence that electronic transport is not very efficient in mixed stack donor:acceptor crystals because of the large separation between equal molecules. (It is tempting to predict that on search for higher mobilities one

should concentrate on aromatic materials with a segregated stacking type packing scheme).

In view of these considerations it is interesting to look at the other directions orthogonal to the z stacking axis. For anthracene:PMDA the x-y cross section of the electron mobility tensor (i.e. the cross section perpendicular to the fast stacking direction) is drawn into a $z \| c$ projection of the crystal structure in Figure 15. The intermediate principal axis of the electron mobility tensor is oriented essentially perpendicular to the (010) cleavage plane (which is perpendicular to the y-axis in the figure); close intermolecular oxygen–oxygen interactions are obviously responsible for the fact that, in spite of the small cohesive interactions in this plane, electron transport is nevertheless more efficient than in the orthogonal direction x. Owing to the crystallographic stacking pattern (the molecular planes are inclined by 21° with respect to the x-y projection (i.e. paper) plane), partial oxygen p_z orbital overlap is possible. The smallness of μ_{11}—despite the laterally extended interaction of the molecules for this direction—must be due the electron withdrawing anhydride side groups (which, as compared to carbon, bear 6 additional positive nuclear charges on the oxygen atoms on either side).

The temperature dependence of the electron mobility is also strongly anisotropic, (cf. Table I and Figure 12); whereas a "band-like" $\mu \sim T^{-1.4}$ relation is measured in the fastest direction, with a power law increase of the mobility with decreasing

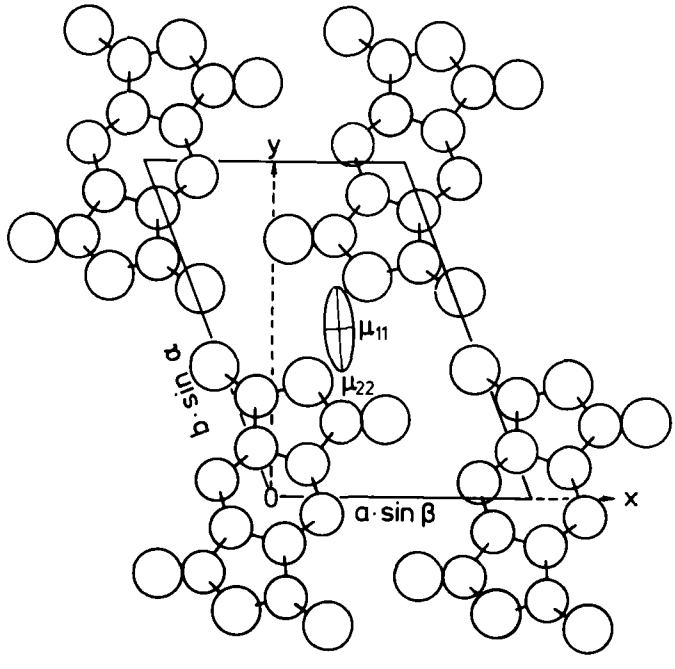

FIGURE 15 Orientation of the electron mobility tensor in the x-y plane relative to the crystallographic environment (plotted with the atomic coordinates and unit cell parameters of Reference 15). The fast component μ_{33} of the electron mobility tensor stands perpendicular to the paper plane and is 50 times greater than the smallest one, μ_{11}

temperature, similar to what has been found for a number of well purified aromatic molecular crystals (cf. e.g. Reference 18), the slowest direction displays a nearly temperature independent electron mobility. This is a striking result! Band-like motion in one crystallographic direction, hopping in another. The intermediate tensor axis, displaying an intermediate magnitude of the mobility as well as an intermediate temperature dependence, $\mu^- \sim T^{-0.9}$, may just be regarded as reflecting an intermediate transport situation; alternatively, and this appears likely, and possible within the experimental error span, it may represent a superposition of both *mechanisms* (not: tensor components!).

A quasi temperature independent electron mobility over a considerable temperature range has been known for μ_{cc}^- in anthracene and naphthalene for a long time[21-23]; other examples of similar behaviour were found for the holes in perylene, the electrons in pyrene (whereas the respective opposite carrier sign displays a "band-like" temperature dependence in these latter two compounds), and for the holes in (orientationally) disordered 2,3-dimethylnaphthalene; (these recent results have been communicated so far in short form only[24]).

Summarizing these results and without going into details it can be noted that in photoconducting aromatic molecular crystals two types of transport behaviour seem to occur independently: a "band-like" $\mu \sim T^n$ $(-3 \leq n \leq -1)$ which can extend *with constant n* over a wide temperature range, e.g. from a few K to 400 K,[6,25] and a polaronic hopping type μ which is nearly temperature independent or very slightly (intrinsically) thermally activated. Whereas the former can be treated in a conventional band theory description with a mean free path of several lattice constants in the low temperature high mobility regime,[25] an understanding of the unaltered extension of the temperature dependence law from there to high temperatures is still a challenging problem; a "nearly small molecular polaron" approach which is based on strong polarization coupling of charge carriers to intramolecular atomic displacements ("vibrons") and which introduces a strongly temperature dependent effective mass in conjunction with a correlated hopping transfer, seems to be able to reconcile a mean free path of only one lattice constant (which has to be assumed at the elevated temperatures) with the observed power law temperature dependence.[26]—For the latter hopping type transport there are several basic approaches in literature, see e.g. Reference 27. More refined models which take into account that in real 3-dimensional systems transport can be band-like in one orientation and hopping in another, or which even give a description of a superposition of the two mentioned, fundamentally different, mechanisms of charge transfer, are at least not in a state of development that would allow making correct predictions on the basis of a mere structural data input.

Hole transport

From the preliminary hole transport data only two conclusions seem appropriate at present:

I) The intrastack hole mobility is very similar to the intrastack electron mobility (at least near room temperature).

II) The anisotropy of the hole mobility is much smaller than that of the electron mobility.—The first observation is at least not surprising since the intrastack donor-

donor distance is the same as the acceptor-acceptor distance, and, moreover, the donor and the acceptor molecules have the same orientation and approximately the same size of the π-electron system. The second fact which is also found in neat naphthalene and anthracene (albeit not so strongly pronounced), indicates that the lateral transfer (i.e. in the *x-y* plane of anthracene:PMDA, corresponding to the situation for the *c'* direction in anthracene and naphthalene) is more efficient for holes than for electrons. We ascribe this to the chemical nature of the laterally "contacting" hydrogen substituents which rather tend to assume a positive partial charge than a negative and hence favour hole transfer.

Nature and origin of the trapping states

We have to deal with an electron trap of "depth" (activation energy) 0.20 eV and concentration $c = 5 \cdot 10^{-5}$ mol/mol, and with a hole trap of $E_{act} = 0.58$ eV and $c = 10^{-6}$ mol/mol. These traps could have either intrinsic origin (Schottky defects, i.e. empty lattice sites; dislocations; stacking faults; stoichiometry defects, which all locally alter the polarization and interaction energies), or be of extrinsic nature (foreign molecules, "impurities"). One characteristic feature of the latter defects, allowing their distinction, is that at least in principle, further purification should lead to further reduction of the concentration. This was indeed observed on comparing the electron mobility results of the highly purified samples measured in this work with the results obtained earlier with less purified material (Figure 8); it is also worth noting that the nature of the residual traps in these completely independent samples is obviously the same, a conclusion which can be drawn from the fact that the activation energies are the same within the experimental error span of approximately ±0.02 eV, while the concentration has been reduced. From this an extrinsic nature of the observed shallow electron traps may be concluded. It is surprising over how wide a temperature interval trapping apparently occurs by only this shallow trap.

In a simple polarization model approach[21a] a chemical impurity acting as a direct electron or hole trap (we do not consider "X-traps"), should bring its electron affinity or ionization energy into play and thus bear a fingerprint for its identification. The 0.58 eV hole trap, for instance, would then require a chemically different molecule with an approximately 0.58 eV smaller ionization energy. This would have to be a strong donor like phenothiazine or TTF; it is difficult to imagine that such a molecule should have been in the starting material, and if so, not have been removed during the extensive purification procedure. Similarly, an electron trap would require a molecule with still higher electron affinity than PMDA (which as a fairly strong acceptor has already an exceptionally large electron affinity). Therefore again it is hard to imagine what that molecule could be and where it could come from. Could it be a stoichiometry defect which was in thermodynamic equilibrium at a certain temperature and than frozen in, and/or, maybe, partially annealed? Depending on whether the crystal was grown by sublimation or from the melt, the equilibrium from temperature and degree of annealing would vary. Stoichiometry defects, i.e. a donor molecule on an acceptor site (and vice versa) are thermodynamically indispensible for reducing the free energy by increasing the

entropy. They necessarily must exist; the only question is at what concentration level. Donor and acceptor stoichiometry defects need not necessarily be present at the same level; in principle there could also exist a deviation from the exact 1:1 composition in one or the other direction, depending on the magnitude of excess donor (or acceptor) concentration in the melt or vapor phase. Therefore the assumption of stoichiometry defects as a cause for the observed electron and hole traps is at least not unreasonable. The very different observed activation energies for electrons and holes can certainly not be traced back to molecular properties in an easy way, but the magnitude of the sign asymmetry is not beyond what might be physically reasonable. It is certainly worth while to invest more work on this very interesting question.

In summary, we have measured for the first time a full intrinsic ("microscopic") charge carrier (electron) mobility tensor in an organic mixed stack donor:acceptor complex crystal and found:

I) a very strong anisotropy, with the highest electron mobility μ^{-}_{33} (330 K) = 0.265 cm^2/Vs occurring along the stacking (and charge transfer) c axis.

II) a temperature dependence $\mu^{-}_{cc} \sim T^{-1.4}$ (320 K $< T <$ 430 K) for the fast axis, whereas the electron mobility in the slowest axis μ^{-}_{11} is temperature independent.

It has been argued that the on stack mobility is of the same "band-like" type as e.g. the electron mobility in perylene (in any direction) and the mobilities of both carrier signs in naphthalene (except for μ^{-}_{cc} above 100 K[18,24]); its smaller magnitude has been ascribed to the larger electron transfer distance to the next equal molecule (acceptor), separated by one inerleaved donor which contributes no resonant states.

These results confirm that in one and the same single crystal a band like and a hopping type transport mechanism can occur simultaneously and that a superposition of both is possible (trivially at least in the non principal directions of the sum mobility tensor).

In addition, preliminary results on hole mobilities were obtained which indicate that along the stacks the hole mobility is similar to the electron mobility (slightly higher), whereas its anisotropy is much less pronounced and its principal axis system differently oriented. These two effects are ascribed to the detailed electron attracting or electron repelling properties of the side groups or atomic ligands which are in van der Waals contact with each other.

We believe that this work presents an illustrative example of how much effort has to be invested if informations on the *intrinsic* transport properties of slightly more complicated organic photoconductors (as compared e.g. with the classical model systems naphthalene or perylene) are wanted.

Acknowledgment

Support by the Stiftung Volkswagenwerk in the program "Physik und Chemie unkonventioneller Materialien" is gratefully acknowledged. Our special thanks are due to M. Gerdon and Ch. Herb, whose enthusiastic cooperation lead to the crystal quality which permitted the measurements presented here to be made.

References

1. H. Möhwald, and D. Haarer, *Mol. Cryst. Liq. Cryst.*, **32**, 215 (1976).
2. Z. Zboinski, *Mol. Cryst. Liq. Cryst.*, **32**, 219 (1976); *idem, phys. stat. sol.*, **b74**, 561 (1976).
3. J. B. Webb, N. S. Dalal, and D. F. Williams, *Mol. Cryst. Liq. Cryst.*, **41**, 203 (1978).
4. D. C. Hoesterey, and G. M. Letson, *J. Phys. Chem. Solids*, **24**, 1609 (1963).
5. N. Karl a) in: H. C. Freyhardt, ed., "Crystals, Growth, Properties and Applications," Vol. 4, (Springer Verlag, Heidelberg 1980), pp. 1–100; b) idem, *Materials Science* (Poland) **10**, 365 (1984).
6. W. Warta, R. Stehle, and N. Karl, *Appl. Phys.*, **A36**, 163 (1985).
7. G. J. Sloan and A. R. McGhie, "Techniques of Melt Crystallization," Vol. XIX of the series: A. Weissberger and W. Sounders, eds., *Techniques of Chemistry*, (John Wiley, New York 1988).
8. N. Karl, and J. Ziegler, *Chem. Phys. Letters*, **32**, 438 (1975).
9. J. Ziegler, and N. Karl, *Chem. Phys.*, **40**, 207 (1979).
10. N. Karl, N. Sato, K. Seki, and H. Inokuchi, *J. Chem. Phys.*, **77**, 4870 (1982).
11. D. Haarer, and N. Karl, *Chem. Phys. Letters*, **21**, 49 (1973).
12. J. Ziegler, Dissertation Thesis, (Universität Stuttgart, FRG, 1979).
13. N. Karl, H. Port, and W. Schrof, *Mol. Cryst. Liq. Cryst.*, **78**, 55 (1981). See also the improved/ augmented version of the Laue program described in: A. Walker, Lehramtsarbeit, 3. Physikalisches Institut der Universität Stuttgart, (Stuttgart, FRG, 1985).
14. J. F. Nye, "Physical Properties of Crystals," (Clarendon Press, Oxford 1972).
15. B. E. Robertson, and J. J. Stezowski, *Acta Cryst.*, **B34**, 3005 (1978).
16. E. A. Silinsh, "Organic Molecular Crystals, Their Electronic States," (Springer Verlag, Berlin 1980).
17. M. Pope, and C. E. Swenberg, "Electronic Processes in Molecular Crystals," (Clarendon Press, Oxford 1982).
18. N. Karl, "Organic Semiconductors," in Landolt-Börnstein, New Series, Subvolume 17i *Semiconductors* (O. Madelung, M. Schulz, and H. Weiss eds.), (Springer Verlag, Berlin 1985).
19. N. Karl, N. Sato, K. Seki, and H. Inokuchi, *J. Chem. Phys.*, **77**, 4870 (1982).
20. E. Prince, L. W. Schroeder, and J. J. Rush, *Acta Cryst.*, **B29**, 184 (1973).
21. a) K. H. Probst, and N. Karl, *Phys. Stat. Sol.*, **a27**, 499, (1975); erratum **a31**, 793 (1975); b) N. Karl, Festkörperprobleme/*Adv. Sol. State Phys.* **14**, 261 (1974).
22. L. B. Schein, *Chem. Phys. Letters*, **48**, 571 (1977).
23. L. B. Schein, C. B. Duke, and A. R. McGhie, *Phys. Rev. Letters*, **40**, 197 (1978).
24. N. Karl, 11th Molecular Crystal Symposium (Lugano 1985), Conference Book pp. 137–142.
25. W. Warta, and N. Karl, *Phys. Rev.*, **32B**, 1172 (1985).
26. E. A. Silinsh, and A. J. Jurgis, *Materials Science* (Poland), **13**, 247 (1987).
27. B. Movaghar, *J. Mol. Electronics*, **3**, 183 (1987) and **4**, 79 (1988).